

ARTICLE

DOI: 10.1038/s41467-018-06190-5

OPEN

Complex strain evolution of polar and magnetic order in multiferroic BiFeO₃ thin films

Zuhuang Chen^{1,2}, Zhanghui Chen³, Chang-Yang Kuo^{4,5}, Yunlong Tang², Liv R. Dedon², Qian Li⁶, Lei Zhang², Christoph Klewe^{3,7}, Yen-Lin Huang², Bhagwati Prasad², Alan Farhan⁷, Mengmeng Yang⁶, James D. Clarkson², Sujit Das², Sasikanth Manipatruni⁸, A. Tanaka⁹, Padraic Shafer⁷, Elke Arenholz⁷, Andreas Scholl⁷, Ying-Hao Chu¹⁰, Z.Q. Qiu⁶, Zhiwei Hu⁴, Liu-Hao Tjeng⁴, Ramamoorthy Ramesh^{2,3,6}, Lin-Wang Wang³ & Lane W. Martin^{2,3}

Electric-field control of magnetism requires deterministic control of the magnetic order and understanding of the magnetoelectric coupling in multiferroics like BiFeO₃ and EuTiO₃. Despite this critical need, there are few studies on the strain evolution of magnetic order in BiFeO₃ films. Here, in (110)-oriented BiFeO₃ films, we reveal that while the polarization structure remains relatively unaffected, strain can continuously tune the orientation of the antiferromagnetic-spin axis across a wide angular space, resulting in an unexpected deviation of the classical perpendicular relationship between the antiferromagnetic axis and the polarization. Calculations suggest that this evolution arises from a competition between the Dzyaloshinskii-Moriya interaction and single-ion anisotropy wherein the former dominates at small strains and the two are comparable at large strains. Finally, strong coupling between the BiFeO₃ and the ferromagnet Co_{0.9}Fe_{0.1} exists such that the magnetic anisotropy of the ferromagnet can be effectively controlled by engineering the orientation of the antiferromagnetic-spin axis.

¹School of Materials Science and Engineering, Harbin Institute of Technology, Shenzhen 518055, China. ²Department of Materials Science and Engineering, University of California, Berkeley, CA 94720, USA. ³Materials Sciences Division, Lawrence Berkeley National Laboratory, Berkeley, CA 94720, USA. ⁴Max-Planck Institute for Chemical Physics of Solids, Nöthnitzer Straße 40, Dresden 01187, Germany. ⁵National Synchrotron Radiation Research Center, 101 Hsin-Ann Road, Hsinchu 30076, Taiwan. ⁶Department of Physics, University of California, Berkeley, CA 94720, USA. ⁷Advanced Light Source, Lawrence Berkeley National Laboratory, Berkeley, CA 94720, USA. ⁸Components Research, Intel Corp., Hillsboro, OR 97124, USA. ⁹Department of Quantum Matter, ADSM, Hiroshima University, Higashi-Hiroshima 739-8530, Japan. ¹⁰Department of Materials Science and Engineering, National Chiao Tung University, Hsinchu 300, Taiwan. These authors contributed equally: Zuhuang Chen, Zhanghui Chen. Correspondence and requests for materials should be addressed to Z.H.C. (email: zuhuang@hit.edu.cn) or to L.W.M. (email: lwmartin@berkeley.edu)

Antiferromagnetic materials play a critical role in the growing field of antiferromagnetic spintronics and more broadly, electric-field control of magnetism¹. Regardless of the applications, knowledge of the antiferromagnetic-spin structure and manipulation of the spin axis are essential for both fundamental understanding of exchange interactions between antiferromagnetic and ferromagnetic layers and for enabling deterministic performance in spintronics^{2,3}. But despite this fact, compared with ferromagnets, there are relatively few studies on controlling the spin structure of antiferromagnets mainly due to the limited probes of spin structure in these materials that lack macroscopic net magnetization.

Among antiferromagnets, BiFeO₃ is particularly interesting because it exhibits robust room-temperature multiferroism (ferroelectricity and antiferromagnetism)^{4,5} and magnetoelectric coupling that allows one to use electric fields to manipulate magnetic order⁶. In turn, researchers have demonstrated the potential for electric-field control of ferromagnetism in exchange-coupled ferromagnet/BiFeO₃ heterostructures, making BiFeO₃ a prime candidate for low-power spintronics and nanoelectronics⁷. Despite this potential, BiFeO₃ is a complex material with many variables that must be controlled. For example, bulk BiFeO₃ has a rhombohedral *R3c* structure with spontaneous polarization (**P**) and antiphase octahedral rotations along the $\langle 111 \rangle$ (pseudocubic indices are used throughout unless otherwise specified), which gives rise to complex domain patterns and switching pathways^{8,9}. The magnetic order of bulk BiFeO₃ crystals is also complex, as it exhibits G-type antiferromagnetism with a superimposed long-wavelength cycloidal modulation along the $\langle 1\bar{1}0 \rangle$ ^{10,11}; that is, the spins rotate within the $\{11\bar{2}\}$ containing the direction of the spontaneous polarization **P** and the cycloid modulation vector^{12,13}. Antiphase oxygen octahedra rotations permit canting of the antiferromagnetic lattice through the Dzyaloshinskii–Moriya interaction (DMI) resulting in a local, weak canted moment **M**^{14,15}, while the spin-cycloid structure results in the cancellation of net macroscopic magnetization and linear magnetoelectric coupling in bulk BiFeO₃^{16–19}. This said, it is reported that epitaxial constraints in thin films can suppress the spin cycloid^{20–22}, and drive a transition toward a homogenous, weakly-ferromagnetic order with a preferred antiferromagnetic spin axis (**L**) in $\{111\}$, which is perpendicular to the oxygen octahedral rotation axis and the direction of **P** (Fig. 1a)^{6,7,23,24}. This can be understood using a phenomenological Hamiltonian consisting of a DMI term and a spin–spin exchange interaction term²³. The DMI term has the form $E_{\text{DM}} = -\mathbf{D} \cdot (\mathbf{L} \times \mathbf{M})$, where E_{DM} is the DMI energy and **D** is the DM vector. Due to symmetry arguments, **D** is determined by the sense of rotation of the oxygen octahedra and is thus oriented along $\langle 111 \rangle$ ²³; i.e., parallel to **P**. A perfect antiferromagnetic order as preferred by the exchange interaction term will have zero DMI energy, while canting of the magnetic moment can make the DMI energy negative, and the most efficient way to have such canting and to reach the lowest energy is when **L** is perpendicular to **D** (and, in turn, **P**)²³. Previous studies, mainly focused on (001)-oriented BiFeO₃ films, reported that compressive strain drives **L** to exhibit the largest out-of-plane component while remaining in the plane perpendicular to **P** (i.e., $[11\bar{2}]$); while tensile strain favors **L** lying in the film plane (i.e., $[1\bar{1}0]$)²⁴. Other studies found a more complex strain evolution of the antiferromagnetic-spin structure, including reports that **L** tends to orient along in-plane $[1\bar{1}0]$ at large compressive strains and along the out-of-plane $[001]$ under tensile strains²⁵. Regardless of the approach, such analyses are complicated by the existence of multiple ferroelastic domains in (001)-oriented films, which could be partially responsible for the diversity of observations^{24,25}. Finally, despite these observations, the mechanism responsible for the strain-induced spin structure

change has not been well developed; precluding further understanding and control of magnetism in BiFeO₃-based heterostructures.

Here, we employ angle- and polarization-dependent soft X-ray absorption spectroscopy (XAS) and X-ray linear dichroism (XLD) together with computational approaches to investigate the influence of epitaxial strain on the antiferromagnetic-spin structure in (110)-oriented BiFeO₃ thin films. We demonstrate from both experiment and theory that, while epitaxial strain has relatively little impact on the orientation of **P**, it can drive a continuous reorientation of **L** from in-plane to out-of-plane directions over a wide angular space, such that **P** and **L** are no longer perpendicular when the films are under tensile strain. Our calculations suggest that spin–spin exchange coupling and the DMI dominate at low strain, giving rise to a perpendicular relationship between **P** and **L**. At large strain values, however, the single-ion anisotropy (SIA) increases in magnitude until it is comparable with the DMI, leading to a gradual deviation of the perpendicular relationship between **P** and **L**. Leveraging the strong exchange coupling between the ferromagnet Co_{0.9}Fe_{0.1} and BiFeO₃, we demonstrate that the anisotropy of the ferromagnet can be tuned by 90° by controlling the strain state of the BiFeO₃. Ultimately, this work provides new insights on the origin of magnetic anisotropy in BiFeO₃ films, demonstrates a pathway to break the expected perpendicular relationship between **P** and **L**, and provides fundamental understanding to enable controllable tuning of spin orientation in BiFeO₃-based heterostructures.

Results

Growth and characterization of (110) BiFeO₃ films with a single structural domain. To understand the effect of epitaxial strain on the antiferromagnetic-spin structure of BiFeO₃, 12–70 nm thick BiFeO₃ films were grown via pulsed-laser deposition on SrTiO₃ (110) and GdScO₃ (010)_O (where the subscript O denotes orthorhombic indices) substrates such that (110)-oriented films are produced (Methods and Supplementary Fig. 1). (110)-oriented films were chosen to reduce the domain variants in BiFeO₃ such that only one **P** and **L** projection on the (110) is possible⁸. For brevity, we focus on four heterostructure variants encompassing two representative BiFeO₃ thicknesses: 12-nm-thick films (which are coherently strained to both the SrTiO₃ and GdScO₃ substrates) and 70-nm-thick films. These show anisotropic strain relaxation such that the films are coherently strained only along the $[001]$ ($[001]_{\text{O}}$) and relaxed along the $[1\bar{1}0]$ ($[100]_{\text{O}}$) for growth on SrTiO₃ (GdScO₃) (Supplementary Fig. 2). Off-axis reciprocal space mapping (Fig. 1b and Supplementary Fig. 2) and piezoresponse force microscopy (Supplementary Fig. 3) studies show that the films are monodomain.

Study of antiferromagnetic spin axis via XLD. The magnetic structure was probed with XLD which arises from two different origins: magnetic-linear dichroism and crystal-field-induced linear dichroism²⁶. In BiFeO₃, temperature-dependent XLD studies have found that the intensity of the XLD signal near T_{N} is much smaller than at 300 K, especially for XLD at the Fe-*L*₂ edge which essentially vanishes (Supplementary Figs. 4 and 5); indicating that the XLD in BiFeO₃ is largely dominated by a magnetic origin²⁷. Representative pairs of XAS (taken in normal incidence with the polarization vector **E** of the incoming X-rays parallel to the $[001]$ (blue curves) and $[1\bar{1}0]$ (red curves); Fig. 1c) and XLD spectra (Fig. 1d) taken on 70-nm-thick BiFeO₃ heterostructures reveal an opposite polarization dependence and a reversal of linear dichroism between films grown on GdScO₃ and SrTiO₃ substrates. The Fe *L*_{2,3} XAS consists of two absorption peaks because of multiplet effects (denoted as *A* and *B*; Fig. 1c), and the spectral

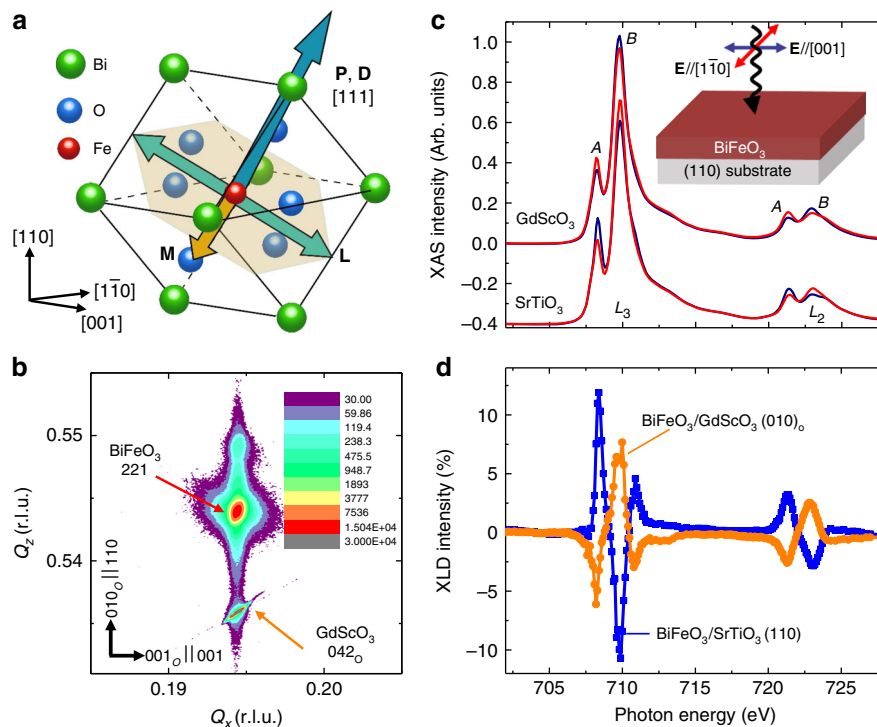


Fig. 1 Strain-induced change in magnetic anisotropy in monodomain BiFeO₃ films. **a** Schematic of a (110)-oriented BiFeO₃ crystal structure wherein the polarization **P**, oxygen octahedral rotation axis **D** (blue arrow), easy-magnetic plane (orange hexagon), antiferromagnetic-spin axis **L** (red arrow), and canted moment **M** (orange arrow) are drawn. **b** Example reciprocal space mapping result, here for a 70-nm-thick BiFeO₃/GdScO₃ (010)_o heterostructure, about the 042_o- (221-) diffraction conditions of GdScO₃ (pseudocubic BiFeO₃). No peak splitting is observed, indicating that the film has single ferroelastic domain structure. **c** Polarization-dependent X-ray absorption spectroscopy (XAS) and **d** X-ray linear dichroism (XLD) spectra at normal incidence about the Fe *L*_{2,3} edge taken on 70-nm-thick BiFeO₃/GdScO₃ (010)_o and SrTiO₃ (110) heterostructures

shape depends on the relative orientation of **E**, the crystallographic axes, and **L**²⁸. The reversed dichroism (Fig. 1d) suggests that the orientation of **L** for these two heterostructures is different.

To better understand the reason for and nature of these changes in the XLD for the different heterostructures, we completed angle- and polarization-dependent XAS studies with various incident X-ray directions for the BiFeO₃ films on both SrTiO₃ and GdScO₃ substrates. The relative angle θ between **E** and a specified crystallographic axis is varied by rotating the samples about the X-ray Poynting vector with different incident angles of the X-rays (Fig. 2a). The L_{2A}/L_{2B} peak intensity ratios, calculated from the XAS as a function of θ , were used to extract the magnetic nature of the films. The L_{2A}/L_{2B} ratio exhibits a strong angle and polarization dependence (Fig. 2b–e), suggesting a uniaxial anisotropy (i.e., an easy axis) in the BiFeO₃ films, since an easy-plane magnetic structure would give rise to a smaller dichroism and weaker angle and polarization dependence²⁴. In addition, the L_{2A}/L_{2B} ratios show a markedly different trend with the polarization angle for the four different film variants (Fig. 2b–e); indicating that strain effectively modifies the orientation of **L**.

To extract the orientation of **L** for the different heterostructure variants, we have simulated the experimental XAS spectra using configuration interaction cluster calculations (Supplementary Figs. 6 and 7)²⁹. For the 12-nm BiFeO₃/GdScO₃ heterostructures (coherently strained to the substrate with a compressive strain of -2% along the $[1\bar{1}0]$ and a tensile strain of 0.1% along $[00\bar{1}]$), the experimental results (points, Fig. 2b) can be well reproduced by simulations with **L** along the in-plane $[1\bar{1}0]$ (lines, Fig. 2b). For the 70-nm BiFeO₃/GdScO₃ heterostructures (relaxed and strained along the $[1\bar{1}0]$ and $[00\bar{1}]$, respectively), the experimental results

(points, Fig. 2c) can be well reproduced by simulations with **L** along the out-of-plane $[110]$ (lines, Fig. 2c). For the 12-nm BiFeO₃/SrTiO₃ heterostructures (coherently strained to the substrate with a compressive strain of -1.4% along both the $[1\bar{1}0]$ and $[00\bar{1}]$), the experimental results (points, Fig. 2d) can be reproduced by simulations with **L** along the in-plane $[00\bar{1}]$ (lines, Fig. 2d). Finally, for the 70-nm BiFeO₃/SrTiO₃ heterostructures (relaxed and strained along the $[1\bar{1}0]$ and $[00\bar{1}]$, respectively), the experimental results (points, Fig. 2e) can be reproduced by simulations with **L** rotated from the in-plane $[00\bar{1}]$ by $\sim 35^\circ$ in the out-of-plane direction (solid lines, Fig. 2e). What these analyses suggest is that, in BiFeO₃, **L** is highly sensitive to the strain state of the material and gradually reorients from in-plane to out-of-plane directions over a wide angular space with increasing tensile strain.

First-principles calculations. To understand the fundamental origin of this strain-driven reorientation of **L**, we performed density functional theory (DFT) calculations (Methods) to explore the evolution of both **L** and **P** under different strains. For each strain state, we calculate the energy landscape when **L** points in different directions (Fig. 3a). In a strain-free film, we find that **L** is energetically degenerate within a plane perpendicular to **P** (here we set **P** to be along the $[111]$); consistent with previous studies²³. Under compressive strain, we find that the easy-plane degeneracy is gradually lifted resulting in **L** continuously rotating to point along the in-plane $[1\bar{1}0]$ at large compressive strains. Under tensile strain, the easy-plane degeneracy also disappears and **L** is gradually changed as the axis first converges to point approximately along the $[11\bar{2}]$. Upon further increasing the magnitude of the tensile strain, **L** rotates toward the out-of-plane $[110]$. The change of **L** with strain is summarized (red lines,

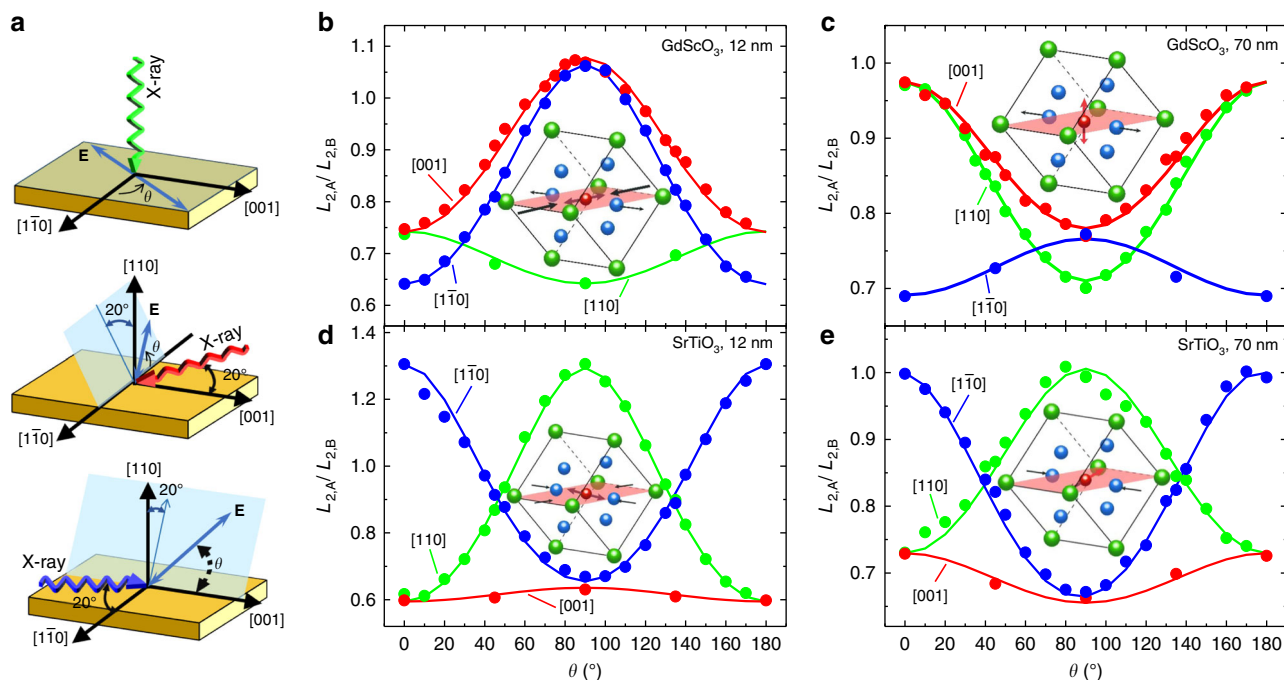


Fig. 2 Angle- and polarization-dependent X-ray absorption spectroscopy. **a** Schematics of the measurement geometries where θ is the angle between the polarization vector \mathbf{E} of the incoming X-rays (blue arrows) and the principal crystallographic axes as labeled. Experimental (solid points) and calculated (lines) show the polarization dependence of the Fe- L_2 -peak ratio as a function of θ for incident X-rays along the $[110]$ (green lines), $[001]$ (red lines), and $[\bar{1}\bar{1}0]$ (blue lines) of **b** 12 nm and **c** 70 nm thick films on GdScO_3 (010)_O, and **d** 12 nm and **e** 70 nm thick films on SrTiO_3 (110). Insets of **(b–e)** show the schematics of the strain states and the orientation of \mathbf{L} (red arrow)

Fig. 3b). Note that the DFT results are calculated at 0 K and the magnetic anisotropy energies (sub meV) are at the resolution of the DFT calculations^{29,30}. Thus, as is common practice, a relatively large strain is used to demonstrate the trend, which agrees well with the experiments.

Having observed that \mathbf{L} rotates in a continuous manner as the strain is varied, this begs the question: Is \mathbf{P} also rotating considerably during application of strain to maintain the classical perpendicular coupling to \mathbf{L} ? To explore this, we have evaluated \mathbf{P} using the Berry-phase method under different strain conditions (Fig. 3c) and find that the in-plane $\mathbf{P}_{[\bar{1}\bar{1}0]}$ component is maintained essentially constant at $\sim 0 \text{ C/m}^2$ while the perpendicular, in-plane $\mathbf{P}_{[001]}$ and out-of-plane $\mathbf{P}_{[110]}$ components increase and decrease in magnitude, respectively, as the strain varies from compressive to tensile in nature. This suggests that \mathbf{P} rotates only by an amount of $\pm 15^\circ$ from the $[111]$ within the $(\bar{1}\bar{1}0)$ (blue lines, Fig. 3b). Importantly, this gradual strain-driven rotation of \mathbf{P} is not synchronized with the rapid rotation of \mathbf{L} (Fig. 3a, b). As a result, \mathbf{P} and \mathbf{L} will no longer be perpendicular under some strain states and the angle between \mathbf{P} and \mathbf{L} will vary nonlinearly with strain starting from 90° and reaching a minimum of 46° at large tensile strains (Fig. 3d). To confirm that the strain-driven polarization rotation is not synchronized with the rotation of \mathbf{L} , we completed polarization mapping with scanning transmission electron microscopy (STEM and Methods) (data shown here for the 70 nm $\text{BiFeO}_3/\text{GdScO}_3$ heterostructure, Fig. 3e). Magnified bright-field images (Fig. 3f) allow for direct measurement of the cation and anion displacements. Polarization maps were produced by extracting these displacements and reveal a uniform polarization direction close to the expected $[111]$ (Fig. 3g and Supplementary Figs. 8 and 9). This observation is further supported by polarization-electric field hysteresis loop measurements, which reveal that the out-of-plane \mathbf{P} of the (110) -oriented films is $\sim 90 \mu\text{C/cm}^2$ (Supplementary Fig. 10), as expected³¹.

Ultimately, this confirms that \mathbf{P} and \mathbf{L} can deviate markedly from the classically expected perpendicular configuration.

Previous studies on the magnetic structure of BiFeO_3 have generally considered only the DMI contribution which is related to the Fe–O–Fe bond angle (inset, Fig. 4a), while the SIA, which is related to the distortion of the FeO_6 octahedra (i.e., Bi–Fe distance³⁰), has been less studied. Using an ab initio derived spin Hamiltonian (Methods and Supplementary Fig. 11), we find that the SIA is very sensitive to the strained-induced lattice distortion and that the change of \mathbf{L} with strain results from a change of the balance between the DMI (as represented by \mathbf{D} , Fig. 4a) and the SIA (as represented by the SIA constant K , Fig. 4b) effects³². When the DMI energy dominates over the SIA energy, the \mathbf{L} and \mathbf{P} will be approximately perpendicular, otherwise, this relationship will be broken. Closer inspection of the trends reveals a number of important observations. At zero strain, K is more than 10-times smaller than \mathbf{D} ³⁰; therefore, the magnetic anisotropy is dictated by the DMI and thus \mathbf{L} is predicted to be constrained within an easy plane perpendicular to \mathbf{D} and, ultimately, \mathbf{P} . It has been reported that when K becomes larger than a critical value, a simple G-type antiferromagnet becomes robust against an incommensurate magnetic structure with an easy-magnetic plane^{30,33}. This is consistent with our calculations wherein the disappearance of the easy-magnetic plane in the strained films can be explained by the enhancement of the K value via strain-induced structural distortion. K is dramatically enhanced in films under large compressive or tensile strain and becomes comparable in magnitude to \mathbf{D} . At large compressive strains, $\mathbf{D}_{[\bar{1}\bar{1}0]}$ is essentially zero, and $\mathbf{D}_{[110]}$ is considerably smaller than $\mathbf{D}_{[00\bar{1}]}$; suggesting that \mathbf{D} is aligned along the $[00\bar{1}]$ (Fig. 4a). Because \mathbf{D} , \mathbf{L} , and \mathbf{M} form a right-handed coordinate relationship, \mathbf{L} will prefer to remain in the (001) . Furthermore, even though $\mathbf{D}_{[110]}$ is small, the fact that it is non-zero breaks any degeneracy and leads

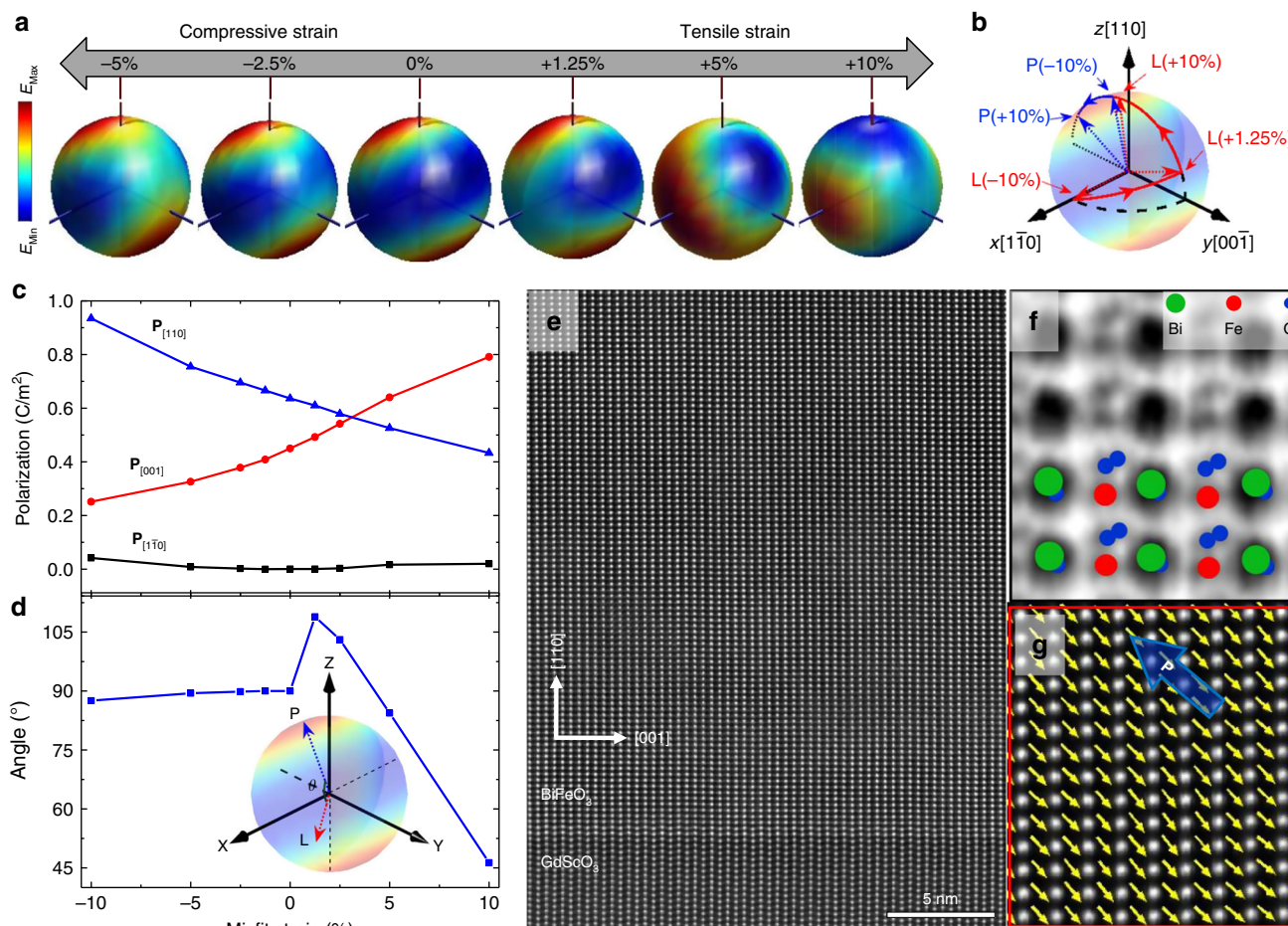


Fig. 3 Evolution of antiferromagnetic-spin and polarization with strain. **a** Three-dimensional representation of the evolution of the magnetic energy landscape under various strain states. The color in the representation indicates the total energy when the antiferromagnetic-spin axis \mathbf{L} points in that direction wherein cool and warm colors represent low and high energy, respectively, and thus easy and hard axes, respectively. **b** Summary of the evolution of antiferromagnetic-spin axis \mathbf{L} (red arrow) and polarization \mathbf{P} (blue arrow) with strain from first-principles calculations. **c** The three components of the polarization as a function of misfit strain from the first-principles calculations. **d** The angle θ between the polarization vector and the antiferromagnetic-easy axis as a function of misfit strain. **e** High-resolution high-angle annular dark field-scanning transmission electron microscopy (HAADF-STEM) image of a 70 nm $\text{BiFeO}_3/\text{GdScO}_3$ $(010)_O$ heterostructure. **f** Bright field-scanning transmission electron microscopy (BF-STEM) image of the same heterostructure showing the Fe cation and O anion displacement details. Direct imaging of all species in the BF-STEM image enables direct extraction of the polar distortions. **g** Fe-cation displacement vector maps relative to its two neighboring Bi cations; the films are found to exhibit uniform structural distortion as noted, indicating that the polar direction of the film is uniform and close to the expected $\langle 111 \rangle$

to \mathbf{L} preferring to point along the in-plane $[1\bar{1}0]$. This is augmented by the SIA since, in the case of compressive strain, the out-of-plane Fe–O bonding strength is weakened while the in-plane term is enhanced, which results in the SIA further driving \mathbf{L} towards the in-plane $[1\bar{1}0]$ ³⁴. At large tensile strains, however, things are more complicated. $\mathbf{D}_{[1\bar{1}0]}$ is again essentially zero, and $\mathbf{D}_{[00\bar{1}]}$ is now marginally larger than $\mathbf{D}_{[110]}$, indicating that \mathbf{D} should be within the $(1\bar{1}0)$, and is driven closer to the $[00\bar{1}]$, thus \mathbf{L} tends to be in the $(00\bar{1})$. Note that K ($\sim 40 \mu\text{eV}$) is also comparable to \mathbf{D} ($< 90 \mu\text{eV}$). Thus under tensile strain, the out-of-plane Fe–O bonding strength is enhanced while the in-plane Fe–O bonding is weakened (Supplementary Fig. 12), meaning that K will rotate out-of-plane, resulting in \mathbf{L} pointing along the out-of-plane $[110]$ rather than in-plane $[1\bar{1}0]$ ³⁴. \mathbf{P} and \mathbf{D} point to the same $[111]$ under zero strain, but they deviate under strain. This is because \mathbf{D} is related to the Fe–O–Fe bonding angle while \mathbf{P} is related to the relative displacement of the positive (Bi, and to a lesser extent, Fe) and negative (O) charge centers which experience only minor changes (Supplementary Fig. 13) under

strain; thus leading to the gradual rotation of \mathbf{P} and its asynchrony with the rotation of \mathbf{L} . The fine sensitivity of SIA to structural distortion may also explain how even small misfit strains in BiFeO_3 films can be sufficient to suppress the spin cycloid^{20–22}.

Controlling magnetic anisotropy of a coupled ferromagnetic layer. Having developed a picture of the fundamental nature of magnetic structure evolution with strain and the underlying mechanism for those changes, we continue to probe the effect of strain-induced antiferromagnetic spin reorientation on the exchange coupling with a ferromagnet. 2.5 nm Pt/2.5 nm $\text{Co}_{0.9}\text{Fe}_{0.1}$ heterostructures were grown on the 70-nm-thick BiFeO_3 films under a field ($H_g = 200 \text{ Oe}$) applied either along the in-plane $[00\bar{1}]$ or $[1\bar{1}0]$ (Methods). Representative magneto-optical Kerr effect (MOKE) hysteresis loops taken from the $\text{Co}_{0.9}\text{Fe}_{0.1}/\text{BiFeO}_3$ heterostructures where H_g was applied along the $[00\bar{1}]$ (Fig. 5a, b) and the $[1\bar{1}0]$ (Supplementary Fig. 15) illustrate that, irrespective of the orientation of H_g , the ferromagnetic easy axis is always along $[00\bar{1}]$ and $[110]$ for the

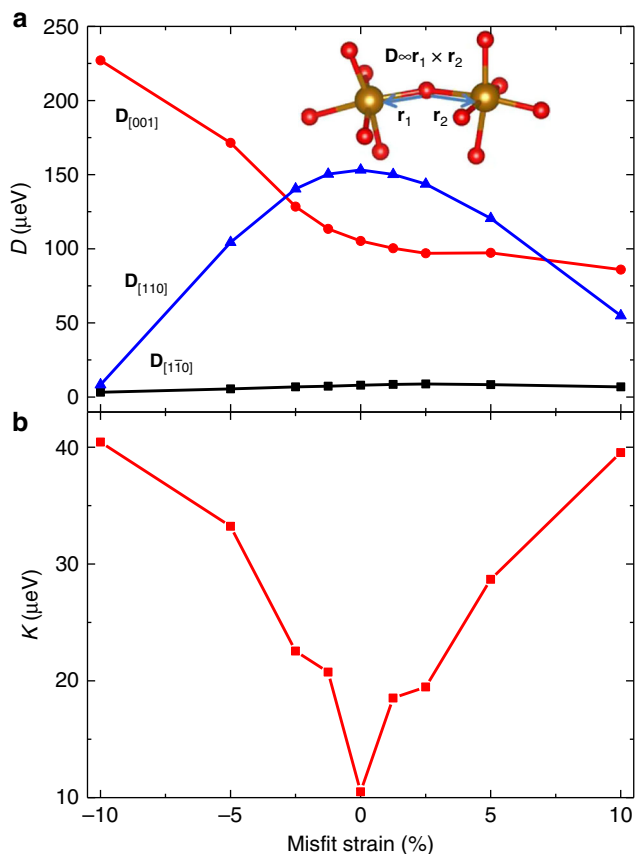


Fig. 4 Magnetic evolution with strain via spin Hamiltonian. **a** Strain dependence of the in-plane ($[1\bar{1}0]$, $[00\bar{1}]$) and out-of-plane ($[110]$) components of the \mathbf{D} vector. Inset shows a schematic of the Dzyaloshinskii-Moriya interaction between two Fe cations (gold) connected by oxygens (red). **b** Strain dependence of the single-ion anisotropy constant K .

heterostructures grown on GdScO_3 (Fig. 5a) and SrTiO_3 (Fig. 5b), respectively. Without the BiFeO_3 layer, the easy axis of the $\text{Co}_{0.9}\text{Fe}_{0.1}$ film is always along the $[00\bar{1}]$ on the two substrates; again irrespective of the direction of H_g (blue and green curves, Fig. 5a, b, and Supplementary Fig. 16). All $\text{Co}_{0.9}\text{Fe}_{0.1}/\text{BiFeO}_3$ heterostructures show an enhancement of the coercive field, compared to $\text{Co}_{0.9}\text{Fe}_{0.1}$ grown on bare substrates, indicating a robust exchange coupling. The small exchange bias observed in our $\text{Co}_{0.9}\text{Fe}_{0.1}/\text{BiFeO}_3$ heterostructures is consistent with previous studies, which suggest that exchange bias is related to pinned uncompensated spins at BiFeO_3 domain walls^{22,35,36}. The angular evolution of the remanent magnetization of the $\text{Co}_{0.9}\text{Fe}_{0.1}$ layers deposited on the BiFeO_3 obtained from the hysteresis loops are plotted in a polar curve (Fig. 5c). Similar to that observed in permalloy/ BiFeO_3 single crystal structures wherein the spin-cycloid structure is present³⁷, the $\text{Co}_{0.9}\text{Fe}_{0.1}$ layers deposited on the BiFeO_3 thin films all present a uniaxial anisotropy; however, the coupling mechanism could be different since the spin cycloid has been suppressed in our films. Interestingly, for heterostructures grown on SrTiO_3 , the exchange coupling between \mathbf{L} and the ferromagnetic spin axis in the $\text{Co}_{0.9}\text{Fe}_{0.1}$ is strong enough to overcome the substrate-asymmetry and growth-field induced anisotropy and set the ferromagnetic spin along the $[1\bar{1}0]$. Since the in-plane projection of \mathbf{L} on SrTiO_3 is along the $[00\bar{1}]$, one can conclude that the BiFeO_3 and $\text{Co}_{0.9}\text{Fe}_{0.1}$ spins are perpendicularly coupled. The perpendicular coupling at the antiferromagnetic/

ferromagnetic interface is due to the spin-flop coupling mechanism. According to the spin-flop mechanism, it is energetically preferred for a small canted moment in the antiferromagnet to couple parallel to the ferromagnetic magnetization, giving rise to a uniaxial magnetic anisotropy in the ferromagnet³⁸. The XLD measurements have also shown that the \mathbf{L} of the 70 nm $\text{BiFeO}_3/\text{GdScO}_3$ heterostructures rotates towards the out-of-plane direction. Thus the in-plane anisotropy is reduced, consistent with magnetic torque results which reveal that the in-plane uniaxial anisotropy constant in heterostructures grown on SrTiO_3 is much larger than those on GdScO_3 (Fig. 5d). All told, our studies demonstrate that a strong exchange coupling between the ferromagnetic $\text{Co}_{0.9}\text{Fe}_{0.1}$ and antiferromagnetic BiFeO_3 exists such that the anisotropy direction of the $\text{Co}_{0.9}\text{Fe}_{0.1}$ is set by the orientation of \mathbf{L} of the underlying BiFeO_3 layer.

Conclusions. In summary, we demonstrate the ability to tune the antiferromagnetic-axis orientation from in-plane to out-of-plane across as wide angular space on (110) -oriented BiFeO_3 thin films via epitaxial strain. A deviation of the classical perpendicular relationship between the antiferromagnetic axis and the polarization vector was found in both experiments and ab initio calculations. This phenomenon arises due to the interplay of the DMI and SIA effects. By engineering the antiferromagnetic-spin orientation, in turn, we can effectively tune the magnetic anisotropy of exchange-coupled $\text{Co}_{0.9}\text{Fe}_{0.1}$ layers. Our results enable a deeper understanding of the magnetic nature of BiFeO_3 and exchange interaction at the BiFeO_3 /ferromagnet interface, and will help to design next-generation spintronic devices, such that electric-field control of magnetic spin orientation may be more readily achieved.

Methods

Sample preparation. Epitaxial BiFeO_3 thin films were grown on SrTiO_3 (110) and GdScO_3 $(010)_O$ single-crystal substrates via pulsed-laser deposition at 680°C in a dynamic oxygen pressure of 100 mTorr³⁹. Following growth, the BiFeO_3 films were cooled in ~ 700 Torr of oxygen to room temperature at a rate of $5^\circ\text{C}/\text{min}$. Detailed structural information was obtained using high-resolution X-ray diffraction (X'Pert MRD Pro, Panalytical) including θ - 2θ scans and reciprocal space maps (RSMs).

Soft X-ray absorption spectroscopy. X-ray spectroscopy measurements were carried out at beamline 4.0.2 of the Advanced Light Source (ALS) at Lawrence Berkeley National Laboratory and beamline 08B of the National Synchrotron Radiation Research Center (NSRRC) in Taiwan. The measurements were performed in total-electron-yield (TEY) geometry. The XLD measurements were obtained from the difference of horizontal and vertical polarized light absorption spectra. The sample temperature was controlled using an in-vacuum resistive heater. After heating to 600 K, we checked the XAS at 300 K again and found no surface degradation caused by the heating (Supplementary Fig. S5). The X-ray beam was incident on the sample at an angle of 20° and 90° from the sample surface for grazing incidence and normal incidence, respectively; the light polarization was selected using an elliptically-polarizing undulator. Spectra were captured with the order of polarization rotation reversed (e.g., horizontal, vertical, and then vertical, horizontal) so as to eliminate experimental artifacts. The angle- and polarization-dependent XAS measurements were independently performed at room temperature for the BiFeO_3 films using TEY geometry at NSRRC. The relative angle θ between light polarization vector \mathbf{E} and the crystallographic axes are varied by rotating the samples about the X-ray Poynting vector. Such experimental geometry allows for the X-ray penetration path length of the incoming beam to be independent of the polarization angle θ , guaranteeing a reliable comparison of the spectral line shapes as a function of θ ⁴⁰.

Configuration interaction cluster calculations. To extract the orientation of the antiferromagnetic axes of the various (110) -oriented BiFeO_3 films, we have simulated the experimental spectra using configuration interaction calculations with the octahedral FeO_6 cluster, based on atomic multiplet theory and the local effects of the solid^{41,42}. It takes into account the intra-atomic $3d$ - $3d$ and $2p$ - $3d$ Coulomb and exchange interactions, the atomic $2p$ and $3d$ spin-orbit coupling of the Fe ion, the oxygen $2p$ -Fe $3d$ hybridization, and the octahedral crystal-field of Fe $3d$ orbital interaction⁴³. The simulations were carried out using the program XTLS 8.3, and the parameters used in the FeO_6 cluster calculations for BiFeO_3 film are:

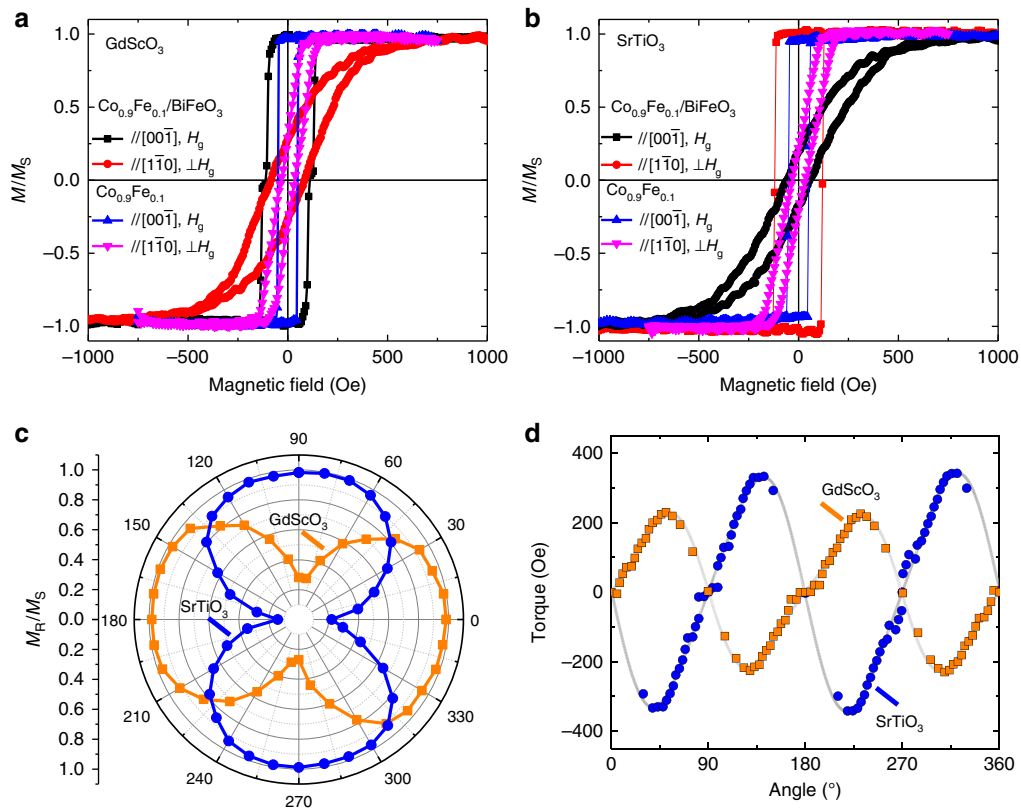


Fig. 5 Controlling ferromagnetic anisotropy. **a** Room temperature magneto-optical Kerr effect (MOKE) hysteresis loops measured in-the-plane of the film for the Pt/Co_{0.9}Fe_{0.1}/BiFeO₃/GdScO₃ (010)_O heterostructures with H_g along [001] and similarly grown Pt/Co_{0.9}Fe_{0.1}/GdScO₃ (010)_O heterostructures. **b** Room temperature MOKE hysteresis loops measured in-the-plane of the film for the Pt/Co_{0.9}Fe_{0.1}/BiFeO₃/SrTiO₃ (110) heterostructures with H_g along [001] and similarly grown Pt/Co_{0.9}Fe_{0.1}/SrTiO₃ (110) heterostructures. **c** Polar plot of the evolution of M_R/M_S for the Pt/Co_{0.9}Fe_{0.1}/BiFeO₃/GdScO₃ (010)_O and SrTiO₃ (110) heterostructures. The angle is defined between the applied field H and the [001]. **d** Magnetic torque as a function of angle of M_R/M_S for the two heterostructures

$\Delta = 2.0$ eV; $U_{dd} = 5.0$ eV; $U_{dp} = 6.0$ eV; $10Dq = 0.8$ eV; $pd\sigma = -1.47$ eV; $pd\pi = 0.68$ eV; and the Slater integrals reduced to 70% of the Hartree-Fock values²⁹.

Scanning transmission electron microscopy. STEM work was performed in National Center for Electron Microscopy (NCEM), Molecular Foundry, Lawrence Berkeley National Laboratory. The samples for the STEM experiments were prepared by slicing, gluing, grinding, dimpling, and, finally, ion milling. Samples were subsequently Ar-ion milled using a Gatan Precision Ion Milling System II (PIPS II) with starting energies of 4 keV stepped down to an energy of 1 keV for the final milling. Before ion milling, the samples were dimpled down to less than 20 μ m. High-angle annular dark field (HAADF)-STEM and bright-field (BF)-STEM imaging was performed on the Cs-corrected TEAM1 FEI Titan microscope at 300 kV. To enable determination of the atomic positions and Fe³⁺ ion displacement vectors, noise in the HAADF images was filtered by Wiener filtering. The atom positions were determined accurately by fitting them as 2D Gaussian peaks by using a Matlab script⁴⁴. The Fe³⁺ ion displacement vector was calculated as a vector between each Fe³⁺ and the center of mass of its two nearest neighbors Bi³⁺.

Co_{0.9}Fe_{0.1} deposition and magnetic properties measurements. For exchange-coupling studies, after the growth of the BiFeO₃ films, they were broken into two pieces and immediately inserted into a vacuum sputtering chamber with a base pressure of 8×10^{-8} Torr. A 2.5 nm Pt/2.5 nm Co_{0.9}Fe_{0.1} bilayer was deposited on the BiFeO₃ films and bare substrates by DC sputtering in 8×10^{-4} Torr of Ar at room temperature with a 20 mT growth field along the in-plane [001] and [110]. Magnetic hysteresis loops and magnetic anisotropy measurements were carried out using the longitudinal MOKE and rotation MOKE^{45,46}.

Ab initio calculations. Ab initio calculations were performed using the projector augmented wave (PAW)^{47,48} formalism and a plane wave basis set, as implemented in the Vienna ab initio simulation package (VASP)^{49,50}. The exchange and correlation potential were treated in the framework of generalized gradient approximation (GGA) of Perdew-Burke-Ernzerhof (PBE)⁵¹. The PAW potentials used explicitly treat 15 valence electrons for bismuth ($5d^{10}6s^26p^3$), 14 for iron ($3p^63d^64s^2$), and 6 for

oxygen ($2s^22p^4$). Local spin-density approximation with an additional Hubbard parameter (LSDA+U) was used for the exchange-correlation functional. The Hubbard parameter U and the exchange interaction J that treat the Fe d electrons were set to $U = 2$ eV and $J = 0$ eV. Spin-orbit coupling (SOC) was included to calculate the non-collinear magnetic energy landscape. For the summation of charge densities over the Brillouin zone, a $3 \times 3 \times 3$ k -point mesh is adopted in the calculation of the total energy and force. The wave functions are expanded in plane waves up to a cutoff of 550 eV and the convergence precision of the total energy is set to be lower than 1×10^{-6} eV. Symmetry was switched off to remove any artificial constraints on the possible spin ordering.

The supercell was made of $2 \times 2 \times 2$ cubic perovskite units, containing 40 atoms in total. Its three axes are [110], [001], and [110], respectively, so as to simulate films of a (110)-oriented material (Supplementary Fig. S9). Under each strain (depicted by the misfit of crystal parameters), the in-plane [110] and [001] axes of supercell are fixed while the out-of-plane [110] axis and the atomic positions are fully relaxed; a conjugate gradient algorithm is used and force precision is lower than 0.005 eV/Å. The polarization vector is evaluated by the Born effective charges using the Berry phase method.

The Hamiltonian containing exchange coupling, DMI, and SIA is written as:

$$H = - \sum_{ij} J_{ij} \mathbf{S}_i \cdot \mathbf{S}_j - \sum_{ij} \mathbf{D}_{ij} \cdot \mathbf{S}_i \times \mathbf{S}_j - K \sum_i |\mathbf{S}_i \cdot \mathbf{n}_i|^2 + H_0 \quad (1)$$

where \mathbf{S}_i is the i th spin vector; J_{ij} is exchange parameter; \mathbf{D}_{ij} is the DMI vector; K is the SIA constant, and $\mathbf{n}_i = (\sin \theta_i \cos \varphi_i, \sin \theta_i \sin \varphi_i, \cos \theta_i)$ is the SIA unit vector in spherical coordinates. H_0 includes all other interactions, such as the lattice elastic energy. Here, we consider only the spin interaction between nearest neighbors. Three different DMI vectors \mathbf{D}_1 , \mathbf{D}_2 , and \mathbf{D}_3 are used for neighborhoods along x , y , and z direction, respectively (Supplementary Fig. 12).

We used the method proposed by Xiang et al.⁵² to calculate the DMI parameters. Specifically, to calculate \mathbf{D}_i^x , we considered four spin configurations, in which the spin of Fe₁ and Fe₂ are oriented along the y and z directions, respectively: (1) $\mathbf{S}_1 = (0, S, 0)$, $\mathbf{S}_2 = (0, 0, S)$; (2) $\mathbf{S}_1 = (0, S, 0)$, $\mathbf{S}_2 = (0, 0, -S)$; (3) $\mathbf{S}_1 = (0, -S, 0)$, $\mathbf{S}_2 = (0, 0, S)$; (4) $\mathbf{S}_1 = (0, -S, 0)$, $\mathbf{S}_2 = (0, 0, -S)$. The spin of the other six atoms are

the same and are along the x direction: $S_{\text{others}} = (S, 0, 0)$. By computing the energy of the four spin configurations, we have:

$$D_1^x = \frac{E_1 + E_4 - E_2 - E_3}{4S^2} \quad (2)$$

The other two components of D_1 and the vectors D_2 and D_3 can be computed similarly. The evolution of the three vectors under strain is plotted (Supplementary Fig. 14). Their average vector $D = |D_i| = (D_1 + D_2 + D_3)/3$ is also plotted (Fig. 3b).

The SIA term is calculated by considering only the Fe ion with spin while all the other ions without spin. We performed constrained calculations with various directions of this isolated spin, so as to resolve the energy surface. The SIA constant K is then fitted to these data points.

Data availability

The data that support the findings of this study are available from the corresponding author upon reasonable request.

Received: 27 December 2017 Accepted: 20 August 2018

Published online: 21 September 2018

References

- Jungwirth, T., Marti, X., Wadley, P. & Wunderlich, J. Antiferromagnetic spintronics. *Nat. Nanotechnol.* **11**, 231–241 (2016).
- Nogués, J. & Schuller, I. K. Exchange bias. *J. Magn. Magn. Mater.* **192**, 203–232 (1999).
- Marti, X. et al. Room-temperature antiferromagnetic memory resistor. *Nat. Mater.* **13**, 367–374 (2014).
- Michel, C., Moreau, J. M., Achenbach, G. D., Gerson, R. & James, W. J. The atomic structure of BiFeO₃. *Solid State Commun.* **7**, 701–704 (1969).
- Fischer, P., Polomska, M., Sosnowska, I. & Szymanski, M. Temperature dependence of the crystal and magnetic structures of BiFeO₃. *J. Phys. Solid State Phys.* **13**, 1931–1940 (1980).
- Zhao, T. et al. Electrical control of antiferromagnetic domains in multiferroic BiFeO₃ films at room temperature. *Nat. Mater.* **5**, 823–829 (2006).
- Heron, J. T. et al. Deterministic switching of ferromagnetism at room temperature using an electric field. *Nature* **516**, 370–373 (2014).
- Chu, Y. H. et al. Domain control in multiferroic BiFeO₃ through substrate vicinity. *Adv. Mater.* **19**, 2662–2666 (2007).
- Baek, S. H. et al. Ferroelastic switching for nanoscale non-volatile magnetoelectric devices. *Nat. Mater.* **9**, 309–314 (2010).
- Sosnowska, I., Peterlinneumaier, T. & Steichele, E. Spiral magnetic ordering in bismuth ferrite. *J. Phys. C: Solid State Phys.* **15**, 4835 (1982).
- Park, J.-G., Le, M. D., Jeong, J. & Lee, S. Structure and spin dynamics of multiferroic BiFeO₃. *J. Phys. Condens. Matter* **26**, 433202 (2014).
- Lebeugle, D. et al. Electric-field-induced spin flop in BiFeO₃ single crystals at room temperature. *Phys. Rev. Lett.* **100**, 227602 (2008).
- Ramazanoglu, M. et al. Local weak ferromagnetism in single-crystalline ferroelectric BiFeO₃. *Phys. Rev. Lett.* **107**, 207206 (2011).
- Dzialoshinskii, I. E. Thermodynamic theory of “weak” ferromagnetism in antiferromagnetic substances. *Sov. Phys. JETP-USSR* **5**, 1259–1272 (1957).
- Moriya, T. Anisotropic superexchange interaction and weak ferromagnetism. *Phys. Rev.* **120**, 91–98 (1960).
- Popov, Y. F. et al. Linear magnetoelectric effect and phase transitions in bismuth ferrite BiFeO₃. *JETP Lett.* **57**, 69–73 (1993).
- Ruette, B. et al. Magnetic-field-induced phase transition in BiFeO₃ observed by high-field electron spin resonance: cycloidal to homogeneous spin order. *Phys. Rev. B* **69**, 064114 (2004).
- Kadomtseva, A., Zvezdin, A., Popov, Y., Pyatakov, A. & Vorob'ev, G. Space-time parity violation and magnetoelectric interactions in antiferromagnets. *JETP Lett.* **79**, 571–581 (2004).
- Fishman, R. S. Orientation dependence of the critical magnetic field for multiferroic BiFeO₃. *Phys. Rev. B* **88**, 104419 (2013).
- Bai, F. M. et al. Destruction of spin cycloid in (111)_c-oriented BiFeO₃ thin films by epitaxial constraint: enhanced polarization and release of latent magnetization. *Appl. Phys. Lett.* **86**, 032511 (2005).
- Bea, H., Bibes, M., Petit, S., Kreisel, J. & Barthelemy, A. Structural distortion and magnetism of BiFeO₃ epitaxial thin films: a Raman spectroscopy and neutron diffraction study. *Philos. Mag. Lett.* **87**, 165–174 (2007).
- Béa, H. et al. Mechanisms of exchange bias with multiferroic BiFeO₃ epitaxial thin films. *Phys. Rev. Lett.* **100**, 017204 (2008).
- Ederer, C. & Spaldin, N. A. Weak ferromagnetism and magnetoelectric coupling in bismuth ferrite. *Phys. Rev. B* **71**, 224103 (2005).
- Holcomb, M. B. et al. Probing the evolution of antiferromagnetism in multiferroics. *Phys. Rev. B* **81**, 134406 (2010).
- Sando, D. et al. Crafting the magnonic and spintronic response of BiFeO₃ films by epitaxial strain. *Nat. Mater.* **12**, 641–646 (2013).
- Haverkort, M. W. et al. Magnetic versus crystal-field linear dichroism in NiO thin films. *Phys. Rev. B* **69**, 020408 (2004).
- Ko, K.-T. et al. Concurrent transition of ferroelectric and magnetic ordering near room temperature. *Nat. Commun.* **2**, 567 (2011).
- Arenholz, E., van der Laan, G., Chopdekar, R. V. & Suzuki, Y. Angle-dependent Ni²⁺ X-ray magnetic linear dichroism: interfacial coupling revisited. *Phys. Rev. Lett.* **98**, 197201 (2007).
- Kuo, C. Y. et al. Single-domain multiferroic BiFeO₃ films. *Nat. Commun.* **7**, 12712 (2016).
- Jeong, J. et al. Temperature-dependent interplay of Dzyaloshinskii–Moriya interaction and single-ion anisotropy in multiferroic BiFeO₃. *Phys. Rev. Lett.* **113**, 107202 (2014).
- Baek, S.-H. et al. The nature of polarization fatigue in BiFeO₃. *Adv. Mater.* **23**, 1621–1625 (2011).
- Weingart, C., Spaldin, N. & Bousquet, E. Noncollinear magnetism and single-ion anisotropy in multiferroic perovskites. *Phys. Rev. B* **86**, 094413 (2012).
- Matsuda, M. et al. Magnetic dispersion and anisotropy in multiferroic BiFeO₃. *Phys. Rev. Lett.* **109**, 067205 (2012).
- Dixit, H., Lee, J. H., Krogel, J. T., Okamoto, S. & Cooper, V. R. Stabilization of weak ferromagnetism by strong magnetic response to epitaxial strain in multiferroic BiFeO₃. *Sci. Rep.* **5**, 12969 (2015).
- Martin, L. W. et al. Nanoscale control of exchange bias with BiFeO₃ thin films. *Nano Lett.* **8**, 2050–2055 (2008).
- Chen, Z. et al. 180° Ferroelectric stripe nanodomains in BiFeO₃ thin films. *Nano Lett.* **15**, 6506 (2015).
- Elzo, M. et al. Coupling between an incommensurate antiferromagnetic structure and a soft ferromagnet in the archetype multiferroic BiFeO₃/cobalt system. *Phys. Rev. B* **91**, 014402 (2015).
- Schulthess, T. C. & Butler, W. H. Consequences of spin-flop coupling in exchange biased films. *Phys. Rev. Lett.* **81**, 4516–4519 (1998).
- Chen, Z. H., Damodaran, A. R., Xu, R., Lee, S. & Martin, L. W. Effect of “symmetry mismatch” on the domain structure of rhombohedral BiFeO₃ thin films. *Appl. Phys. Lett.* **104**, 182908 (2014).
- Csizar, S. I. et al. Controlling orbital moment and spin orientation in CoO layers by strain. *Phys. Rev. Lett.* **95**, 187205 (2005).
- de Groot, F. M. F. X-ray absorption and dichroism of transition metals and their compounds. *J. Electron Spectrosc. Relat. Phenom.* **67**, 529–622 (1994).
- Tanaka, A. & Jo, T. Resonant 3d, 3p and 3s photoemission in transition metal oxides predicted at 2p threshold. *J. Phys. Soc. Jpn.* **63**, 2788–2807 (1994).
- Bocquet, A. E. et al. Electronic structure of early 3d-transition-metal oxides by analysis of the 2p core-level photoemission spectra. *Phys. Rev. B* **53**, 1161–1170 (1996).
- Anthony, S. M. & Granick, S. Image analysis with rapid and accurate two-dimensional Gaussian fitting. *Langmuir* **25**, 8152–8160 (2009).
- Li, J. et al. Design of a vector magnet for the measurements of anisotropic magnetoresistance and rotational magneto-optic Kerr effect. *Rev. Sci. Instrum.* **83**, 033906 (2012).
- Li, Q. et al. Electrical switching of the magnetic vortex circulation in artificial multiferroic structure of Co/Cu/PMN-PT(011). *Appl. Phys. Lett.* **110**, 262405 (2017).
- Blöchl, P. E. Projector augmented-wave method. *Phys. Rev. B* **50**, 17953–17979 (1994).
- Kresse, G. & Joubert, D. From ultrasoft pseudopotentials to the projector augmented-wave method. *Phys. Rev. B* **59**, 1758–1775 (1999).
- Kresse, G. & Hafner, J. Ab initio molecular dynamics for liquid metals. *Phys. Rev. B* **47**, 558–561 (1993).
- Kresse, G. & Furthmüller, J. Efficient iterative schemes for ab initio total-energy calculations using a plane-wave basis set. *Phys. Rev. B* **54**, 11169–11186 (1996).
- Perdew, J. P., Burke, K. & Ernzerhof, M. Generalized gradient approximation made simple. *Phys. Rev. Lett.* **77**, 3865–3868 (1996).
- Xiang, H. J., Kan, E. J., Wei, S.-H., Whangbo, M. H. & Gong, X. G. Predicting the spin-lattice order of frustrated systems from first principles. *Phys. Rev. B* **84**, 224429 (2011).

Acknowledgements

The authors thank Prof. P. Yu for fruitful discussions. This work was funded by the U.S. Department of Energy, Office of Science, Office of Basic Energy Sciences, Materials Sciences and Engineering Division under Contract No. DE-AC02-05-CH11231 within the Materials Project program KC23MP for the synthesis of complex-oxide functional materials, the Non-Equilibrium Magnetic Materials program (MSMAG) for the first-principles calculations, and the van der Waals heterostructures program (KCWF16) for the magnetic studies of materials. This research used resources of the Advanced

Light Source, which is a DOE Office of Science User Facility under contract no. DE-AC02-05CH11231. STEM work at the Molecular Foundry was supported by the Office of Science, Office of Basic Energy Sciences, of the U.S. Department of Energy under Contract No. DE-AC02-05CH11231. This research used the resources of the National Energy Research Scientific Computing Center (NERSC) and Oak Ridge Leadership Computing Facility (OLCF) that are supported by the Office of Science of the U.S. Department of Energy, with the computational time allocated by the Innovative and Novel Computational Impact on Theory and Experiment (INCITEE) project. The study of multiferroic thin film devices was supported by the Army Research Office under grant W911NF-14-1-0104. L.R.D. acknowledges support U.S. Department of Energy, Office of Science, Office of Basic Energy Sciences under Award Number DE-SC-0012375. L.W.M. & R.R. acknowledge support from the Gordon and Betty Moore Foundation's EPiQS Initiative, Grant GBMF5307 and Intel, Corp. Z.H.C. acknowledges a startup grant from Harbin Institute of Technology, Shenzhen, China, under project number DD45001017.

Author contributions

Z.H.C. conceived of and designed the research, and analyzed the results with R.R. and L.W.M. Z.H.C. and L.R.D. synthesized the samples. Z.H.C. performed the X-ray structural characterizations and PFM studies. The MOKE-based magnetic properties measurements were carried out by Z.H.C. with the assistance of Q.L., M.M.Y. and Z.Q.Q. Z.H.C., C.Y.K., A.F., L.Z. and C.K. performed the soft X-ray spectroscopy measurements with the assistance of P.S., E.A. and A.S., and interpreted the data with Z.W.H. and L.-H.T. Y.L.T. performed the STEM experiments and analyzed the data. Z.C. and L.-W.W. contributed to the theoretical studies. Z.H.C. and L.W.M. prepared the manuscript with the assistance of Z.C. and L.-W.W. All authors read and contributed to the manuscript and the interpretation of the data.

Additional information

Supplementary Information accompanies this paper at <https://doi.org/10.1038/s41467-018-06190-5>.

Competing interests: The authors declare no competing interests.

Reprints and permission information is available online at <http://npg.nature.com/reprintsandpermissions/>

Publisher's note: Springer Nature remains neutral with regard to jurisdictional claims in published maps and institutional affiliations.



Open Access This article is licensed under a Creative Commons Attribution 4.0 International License, which permits use, sharing, adaptation, distribution and reproduction in any medium or format, as long as you give appropriate credit to the original author(s) and the source, provide a link to the Creative Commons license, and indicate if changes were made. The images or other third party material in this article are included in the article's Creative Commons license, unless indicated otherwise in a credit line to the material. If material is not included in the article's Creative Commons license and your intended use is not permitted by statutory regulation or exceeds the permitted use, you will need to obtain permission directly from the copyright holder. To view a copy of this license, visit <http://creativecommons.org/licenses/by/4.0/>.

© The Author(s) 2018